

# SILVERRUSH. II. First Catalogs and Properties of $\sim 2,000$ $\text{Ly}\alpha$ Emitters and Blobs at $z \sim 6 - 7$ Identified over the $14 - 21 \text{ deg}^2$ Sky

Takatoshi Shibuya<sup>1</sup>, Masami Ouchi<sup>1,2</sup>, Akira Konno<sup>1,3</sup>, Ryo Higuchi<sup>1,4</sup>,  
Yuichi Harikane<sup>1,4</sup>, Yoshiaki Ono<sup>1</sup>, Kazuhiro Shimasaku<sup>3,5</sup>, Yoshiaki  
Taniguchi<sup>6</sup>, Masakazu A. R. Kobayashi<sup>7</sup>, Masaru Kajisawa<sup>8</sup>, Tohru  
Nagao<sup>8</sup>, Hisanori Furusawa<sup>9</sup>, Tomotsugu Goto<sup>10</sup>, Nobunari Kashikawa<sup>9,11</sup>,  
Yutaka Komiyama<sup>9,11</sup>, Haruka Kusakabe<sup>3</sup>, Chien-Hsiu Lee<sup>12</sup>, Rieko  
Momose<sup>10</sup>, Kimihiko Nakajima<sup>13</sup>, Masayuki Tanaka<sup>9,11</sup>, Shiang-Yu Wang<sup>14</sup>,  
and Suraphong Yuma<sup>15</sup>

<sup>1</sup>Institute for Cosmic Ray Research, The University of Tokyo, 5-1-5 Kashiwanoha, Kashiwa, Chiba 277-8582, Japan

<sup>2</sup>Kavli Institute for the Physics and Mathematics of the Universe (Kavli IPMU, WPI), University of Tokyo, Kashiwa, Chiba 277-8583, Japan

<sup>3</sup>Department of Astronomy, Graduate School of Science, The University of Tokyo, 7-3-1 Hongo, Bunkyo, Tokyo 113-0033, Japan

<sup>4</sup>Department of Physics, Graduate School of Science, The University of Tokyo, 7-3-1 Hongo, Bunkyo, Tokyo 113-0033, Japan

<sup>5</sup>Research Center for the Early Universe, Graduate School of Science, The University of Tokyo, 7-3-1 Hongo, Bunkyo, Tokyo 113-0033, Japan

<sup>6</sup>The Open University of Japan, Wakaba 2-11, Mihama-ku, Chiba 261-8586, Japan

<sup>7</sup>Faculty of Natural Sciences, National Institute of Technology, Kure College, 2-2-11 Agaminami, Kure, Hiroshima 737-8506, Japan

<sup>8</sup>Research Center for Space and Cosmic Evolution, Ehime University, Bunkyo-cho 2-5, Matsuyama 790-8577, Japan

<sup>9</sup>National Astronomical Observatory, Mitaka, Tokyo 181-8588, Japan

<sup>10</sup>Institute of Astronomy, National Tsing Hua University, 101 Section 2, Kuang-Fu Road, Hsinchu 30013, Taiwan

<sup>11</sup>The Graduate University for Advanced Studies (SOKENDAI), 2-21-1 Osawa, Mitaka, Tokyo 181-8588

<sup>12</sup>Subaru Telescope, NAOJ, 650 N Aohoku Pl., Hilo, HI 96720, USA

<sup>13</sup>European Southern Observatory, Karl-Schwarzschild-Str. 2, D-85748, Garching bei Munchen, Germany

<sup>14</sup>Academia Sinica, Institute of Astronomy and Astrophysics, 11F of AS/NTU Astronomy-Mathematics Building, No.1, Sec. 4, Roosevelt Rd, Taipei 10617, Taiwan

<sup>15</sup>Department of Physics, Faculty of Science, Mahidol University, Bangkok 10400, Thailand

<sup>‡</sup>Based on data obtained with the Subaru Telescope. The Subaru Telescope is operated by

the National Astronomical Observatory of Japan.

\*E-mail: shibyat@icrr.u-tokyo.ac.jp

Received (reception date); Accepted (acceptation date)

## Abstract

We present an unprecedentedly large catalog consisting of  $2,354 \gtrsim L^*$  Ly $\alpha$  emitters (LAEs) at  $z = 5.7$  and  $6.6$  on the  $13.8$  and  $21.2$  deg $^2$  sky, respectively, that are identified by the SILVERRUSH program with the first narrowband imaging data of the Hyper Suprime-Cam (HSC) survey. We confirm that the LAE catalog is reliable on the basis of 97 LAEs whose spectroscopic redshifts are already determined by this program and the previous studies. This catalogue is also available on-line. Based on this catalogue, we derive the rest-frame Ly $\alpha$  equivalent-width distributions of LAEs at  $z = 5.7$  and  $6.6$  that are reasonably explained by the exponential profiles with the scale lengths of  $72 \pm 19$  and  $119 \pm 4$  Å, respectively, showing the increase trend towards high- $z$ . We find that  $\sim 700$  LAEs with a large equivalent width (LEW) of  $\gtrsim 240$  Å are candidates of young-metal poor galaxies and AGNs. We also find that the fraction of LEW LAEs to all ones is moderately large,  $\sim 30\%$ . Our LAE catalog includes 11 Ly $\alpha$  blobs (LABs) that are LAEs with spatially extended Ly $\alpha$  emission whose profile is clearly distinguished from those of stellar objects at the  $\gtrsim 3\sigma$  level. The number density of the LABs at  $z = 6 - 7$  is  $\sim 10^{-7} - 10^{-6}$  Mpc $^{-3}$ , being  $\sim 10 - 100$  times lower than those claimed for LABs at  $z \simeq 2 - 3$ , suggestive of disappearing LABs at  $z \gtrsim 6$ , albeit with the different selection methods and criteria for the low and high- $z$  LABs.

**Key words:** early universe — galaxies: formation — galaxies: high-redshift

## 1 Introduction

Ly $\alpha$  Emitters (LAEs) are one of important populations of high- $z$  star-forming galaxies in the paradigm of the galaxy formation and evolution. Such galaxies are thought to be typically young (e.g., Gawiser et al. 2007; Finkelstein et al. 2007), compact (e.g., Taniguchi et al. 2009; Bond et al. 2012), less-massive (e.g., Ono et al. 2010; Guaita et al. 2011), metal-poor (e.g., Nakajima et al. 2012; Nakajima et al. 2013; Nakajima & Ouchi 2014; Kojima et al. 2016), less-dusty (e.g., Blanc et al. 2011; Kusakabe et al. 2015), and a possible progenitor of Milky Way mass galaxies (e.g., Dressler et al. 2011). In addition, LAEs are used to probe the cosmic reionization, because ionizing photons escaped from a large number of massive stars formed in LAEs contribute to the ionization of intergalactic medium (IGM; e.g., Shimasaku et al. 2006; Kashikawa et al. 2006; Ouchi et al. 2008; Ouchi et al. 2010; Cowie et al. 2010; Hu et al. 2010; Kashikawa et al. 2011; Shibuya et al. 2012; Konno et al. 2014; Matthee et al. 2015; Matthee et al. 2015; Ota et al. 2017; Zheng et al. 2017).

LAEs have been surveyed by imaging observations with dedicated narrow-band (NB) filters for a prominent redshifted Ly $\alpha$  emission (e.g., Ajiki et al. 2002; Malhotra & Rhoads 2004; Kodaira et al. 2003; Taniguchi et al. 2005; Gronwall et al. 2007; Erb et al. 2011; Ciardullo et al. 2012). In large LAE sample constructed by the NB observations, two rare Ly $\alpha$ -emitting

populations have been identified: large equivalent width (LEW) LAEs, and spatially extended Ly $\alpha$  LAEs, Ly $\alpha$  blobs (LABs).

LEW LAEs are objects with a large Ly $\alpha$  equivalent width (EW) of  $\gtrsim 240$  Å which are not reproduced with the normal Salpeter stellar initial mass function (e.g., Malhotra & Rhoads 2002). Such an LEW is expected to be originated from complicated physical processes such as (i) photoionization by young and/or low-metallicity star-formation, (ii) photoionization by AGN, (iii) photoionization by external UV sources (QSO fluorescence), (iv) collisional excitation due to strong outflows (shock heating), (v) collisional excitation due to gas inflows (gravitational cooling), and (vi) clumpy ISM (see e.g., Hashimoto et al. 2017). The highly-complex radiative transfer of Ly $\alpha$  in the interstellar medium (ISM) makes it difficult to understand the Ly $\alpha$  emitting mechanism (Neufeld 1991; Hansen & Oh 2006; Finkelstein et al. 2008; Laursen et al. 2013; Laursen et al. 2009; Laursen & Sommer-Larsen 2007; Zheng et al. 2010; Yajima et al. 2012; Duval et al. 2013; Zheng & Wallace 2013).

LABs are spatially extended Ly $\alpha$  gaseous nebulae in the high- $z$  Universe (e.g., Steidel et al. 2000; Matsuda et al. 2004; Matsuda et al. 2009; Matsuda et al. 2011; Cantalupo et al. 2014; Arrigoni Battaia et al. 2015b; Hennawi et al. 2015; Arrigoni Battaia et al. 2015a; Cai et al. 2017). The origins of LABs (LAEs with a diameter  $\simeq 20 - 400$  kpc) are

also explained by several mechanisms: (1) resonant scattering of Ly $\alpha$  photons emitted from central sources in dense and extended neutral hydrogen clouds (e.g., Hayes et al. 2011), (2) cooling radiation from gravitationally heated gas in collapsed halos (e.g., Haiman et al. 2000), (3) shock heating by galactic superwind originated from starbursts and/or active galactic nucleus (AGN) activity (e.g., Taniguchi & Shioya 2000), (4) galaxy major mergers (e.g., Yajima et al. 2013), and (5) photoionization by external UV sources (QSO fluorescence; e.g., Cantalupo et al. 2005). Moreover, LABs have been often discovered in over-density regions at  $z \simeq 2 - 3$  (e.g., Yang et al. 2009; Yang et al. 2010; Matsuda et al. 2011). Thus, such LABs could be closely related to the galaxy environments, and might be linked to the formation mechanisms of central massive galaxies in galaxy protoclusters.

During the last decades, Suprime-Cam (SCam) on the Subaru telescope has led the world on identifying such rare Ly $\alpha$ -emitting populations at  $z \gtrsim 6$  (LEW LAEs; e.g., Nagao et al. 2008; Kashikawa et al. 2012; LABs; e.g., Ouchi et al. 2009; Sobral et al. 2015). However, the formation mechanisms of these rare Ly $\alpha$ -emitting populations are still controversial due to the small statistics. While LEW LAEs and LABs at  $z \simeq 2 - 5$  have been studied intensively with a sample of  $\gtrsim 100$  sources, only a few sources have been found so far at  $z \gtrsim 6$ . Large-area NB data are required to carry out a statistical study on LEW LAEs and LABs at  $z \gtrsim 6$ .

In March 2014, the Subaru telescope has started a large-area NB survey using a new wide-FoV camera, Hyper Suprime-Cam (HSC) in a Subaru strategic program (SSP; Aihara et al. 2017b). In the five-year project, HSC equipped with four NB filters of NB387, NB816, NB921, and NB101 will survey for LAEs at  $z \simeq 2.2, 5.7, 6.6$ , and  $7.3$ , respectively. The HSC SSP NB survey data consist of two layers; ultradeep (UD), and deep (D), covering 2 fields (UD-COSMOS, UD-SXDS), and 4 fields (D-COSMOS, D-SXDS, D-DEEP23, D-ELAISN1), respectively. The NB816, NB921, and NB101 images will be taken for the UD fields. The NB387, NB816, and NB921 observations will be conducted in 15 HSC-pointing D fields.

Using the large HSC NB data complemented by optical and NIR spectroscopic observations, we launch a research project for Ly $\alpha$ -emitting objects: *Systematic Identification of LAEs for Visible Exploration and Reionization Research Using Subaru HSC (SILVERRUSH)*. The large LAE samples provided by SILVERRUSH enable us to investigate e.g., LAE clustering (Ouchi et al. 2017), LEW LAEs and LABs (this work), spectroscopic properties of bright LAEs (Shibuya et al. 2017b), Ly $\alpha$  luminosity functions (Konno et al. 2017), and LAE over-density (R. Higuchi et al. in preparation). The LAE survey strategy is given by Ouchi et al. (2017). This program is one of the twin programs. Another program is the study for dropouts, Great Optically Luminous Dropout Research Using

Subaru HSC (GOLDRUSH), that is detailed in Ono et al. (2017); Harikane et al. (2017).

This is the second paper in the SILVERRUSH project. In this paper, we present LAE selection processes and machine-readable catalogs of the LAE candidates at  $z \simeq 5.7 - 6.6$ . Using the large LAE sample obtained with the first HSC NB data, we examine the redshift evolutions of Ly $\alpha$  EW distributions and LAB number density. This paper has the following structure. In Section 2, we describe the details of the SSP HSC data. Section 3 presents the LAE selection processes. In Section 4, we check the reliability of our LAE selection. Section 5 presents Ly $\alpha$  EW distributions and LABs at  $z \simeq 6 - 7$ . In Section 6, we discuss the physical origins of LEW LAEs and LABs. We summarize our findings in Section 7.

Throughout this page, we adopt the concordance cosmology with  $(\Omega_m, \Omega_\Lambda, h) = (0.3, 0.7, 0.7)$  (Planck Collaboration et al. 2016). All magnitudes are given in the AB system (Oke & Gunn 1983).

## 2 HSC SSP Imaging Data

We use the HSC SSP S16A data products of broadband (BB; Kawanomoto 2017) and NB (Ouchi et al. 2017) images that are obtained in 2014-2016. It should be noted that this HSC SSP S16A data is significantly larger than the one of the first-data release in Aihara et al. (2017a). The NB921 (NB816) filter has a central wavelength of  $\lambda_c = 9210\text{\AA}$  (8160\AA) and an FWHM of  $\Delta\lambda = 131\text{\AA}$  (120\AA), which traces the redshifted Ly $\alpha$  emission line at  $z = 6.57 \pm 0.05$  ( $z = 5.71 \pm 0.05$ ). The transmission curves and the detailed specifications of these filters are given in Ouchi et al. (2017).

Table 1 summarizes the survey areas, exposure time, and depth of the HSC SSP S16A NB data. The current HSC SSP S16A NB data covers UD-COSMOS, UD-SXDS, D-COSMOS, D-DEEP23, D-ELAISN1 for  $z \simeq 6.6$ , and UD-COSMOS, UD-SXDS, D-DEEP23, D-ELAISN1 for  $z \simeq 5.7$ . The effective survey areas of the NB921 and NB816 images are 21.2 and 13.8 arcmin<sup>2</sup>, corresponding to the survey volumes of  $\simeq 1.9 \times 10^7$  and  $\simeq 1.2 \times 10^7$  Mpc<sup>3</sup>, respectively. The typical limiting magnitudes of BB filters are  $g \simeq 26.9$ ,  $r \simeq 26.5$ ,  $r \simeq 26.3$ ,  $z \simeq 25.7$ , and  $y \simeq 25.0$  ( $g \simeq 26.6$ ,  $r \simeq 26.1$ ,  $r \simeq 25.9$ ,  $z \simeq 25.2$ , and  $y \simeq 24.4$ ) in a 1''5 aperture at  $5\sigma$  for the UD (D) fields. The FWHM size of point spread function in the HSC images is typically  $\simeq 0''.8$  (Aihara et al. 2017a).

The HSC images were reduced with the HSC pipeline, hscPipe 4.0.2 (Bosch et al. 2017) which is a code from the Large Synoptic Survey Telescope (LSST) software pipeline (Ivezic et al. 2008; Axelrod et al. 2010; Jurić et al. 2015). The HSC pipeline performs CCD-by-CCD reduction, calibration for astrometry, and photometric zero point determination. The pipeline then conducts mosaic-stacking that com-

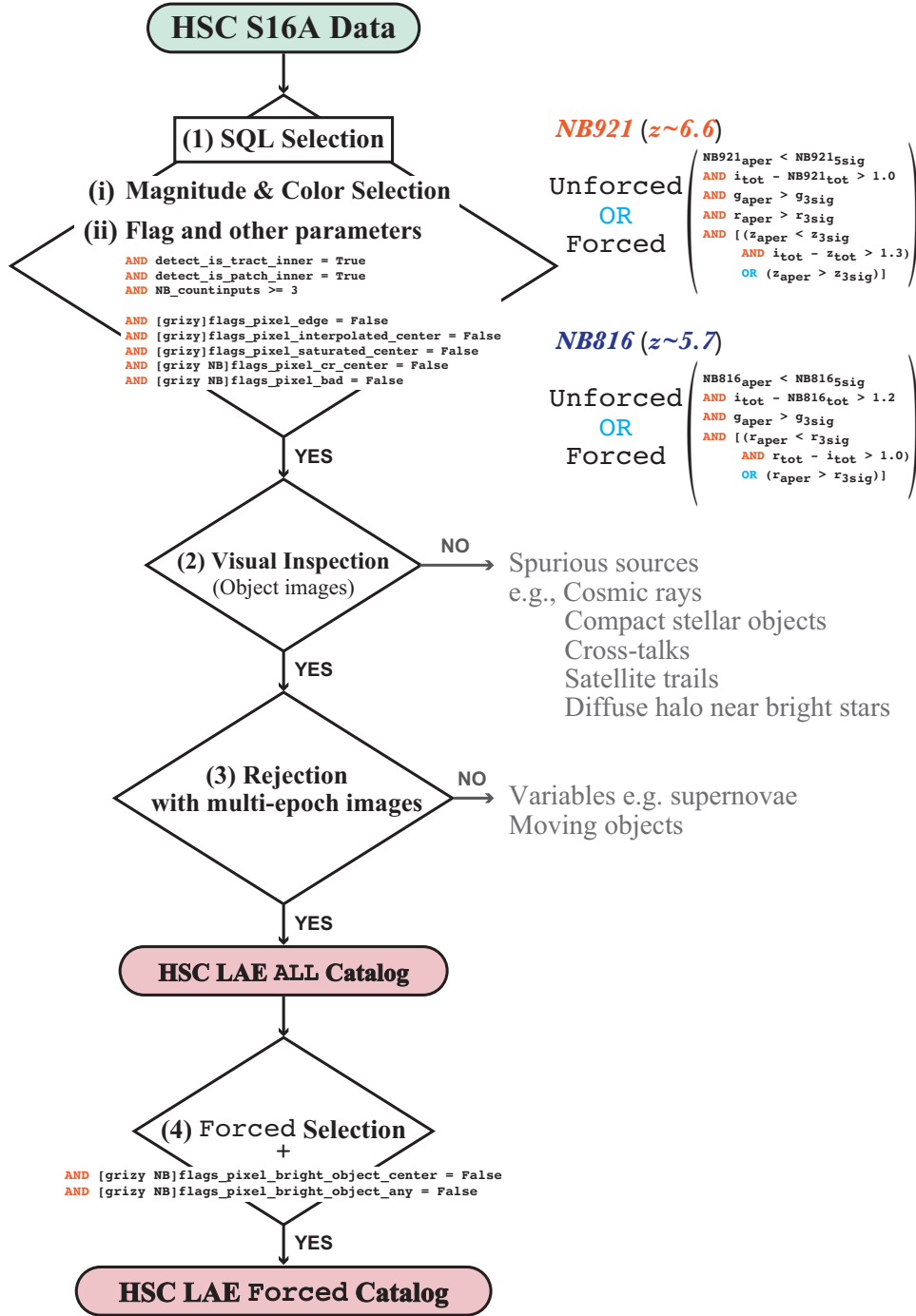
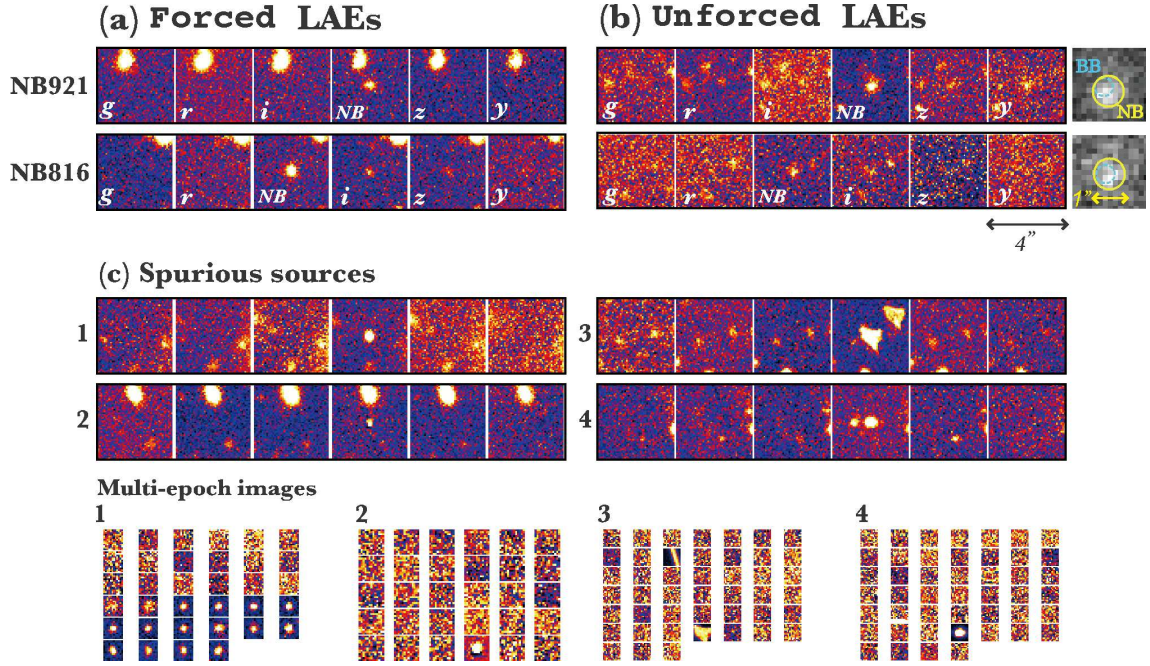


Fig. 1. Flow chart of the HSC LAE selection process. See Section 3 for more details.

bins reduced CCD images into a large coadd image, and create source catalogs by detecting and measuring sources on the coadd images. The photometric calibration is carried out with the PanSTARRS1 processing version 2 imaging survey data (Magnier et al. 2013; Schlafly et al. 2012; Tonry et al. 2012). The details of the HSC SSP survey, data reduction, and source detection and photometric catalog construction are provided in Aihara et al. (2017a); Bosch et al. (2017); Takada et al. (2017).

In the HSC images, source detection and photometry were carried out in two methods: *unforced* and *forced*. The *unforced* photometry is a method to perform measurements of coordinates, shapes, and fluxes individually in each band image for an object. The *forced* photometry is a method to carry out photometry by fixing centroid and shape determined in a reference band and applying them to measure fluxes in all the other bands. The algorithm of the forced detection and photometry





**Fig. 2.** Multi-band cutout images of our example LAEs and spurious sources. (a) LAEs at  $z \simeq 6.6$  (top) and  $z \simeq 5.7$  (bottom) in the forced LAE catalog. (b) LAEs at  $z \simeq 6.6$  (top) and  $z \simeq 5.7$  (bottom) in the unforced catalog. In the rightmost cutout images, the yellow solid and cyan dashed circles represent the central positions of the unforced LAEs in the NB and BB images, respectively. The diameters of the yellow solid and dashed circles in the cutout images of the unforced LAEs are  $1''$  and  $0.75''$ , respectively. (c) Spurious sources with an NB magnitude-excess similar to that of LAE candidates (four panel sets at the top), 1: variable (e.g., supernova); 2: cosmic ray; 3: cross-talk artifact; 4: moving object (e.g., asteroids) and corresponding multi-epoch images (four panel sets at the bottom). The image size is  $4'' \times 4''$  for the LAEs and spurious sources.

is similar to the double-image mode of SExtractor (Bertin & Arnouts 1996) that are used in most of the previous studies for high- $z$  galaxies. According to which depends on magnitudes,  $S/N$ , positions, and profiles for detected sources, a BB filter is regarded as a reference band. We refer the detailed algorithm to choose the reference filter and filter priority to Bosch et al. (2017). In this study, we use both samples of LAEs selected in either color criteria of  $BB - NB$  defined by the unforced or forced magnitudes to identify objects with a large spatial offset between the Ly $\alpha$  and UV continuum emission (e.g., Shibuya et al. 2014).

We use *cmodel* magnitudes for estimating total magnitudes of sources. The *cmodel* magnitude is a weighted combination of exponential and de Vaucouleurs fits to the light profile of each object. The detailed algorithm of the *cmodel* photometry are presented in Bosch et al. (2017). To measure the  $S/N$  values for source detections, we use  $1.5''$ -diameter aperture magnitudes.

### 3 LAE Selection

Using the HSC data, we perform a selection for LAEs at  $z \simeq 6.6$  and  $z \simeq 5.7$ . Basically, we select objects showing a significant flux excess in the NB images and a spectral break at the wavelength of redshifted Ly $\alpha$  emission. Figure 1 shows the flow chart of the LAE selection process. We carry out the following

processes: (1) SQL selection, (2) visual inspections for the object images, (3) rejections of variable and moving objects with the multi-epoch images, and (4) forced selection. The details are described as follows.

- (1) **SQL selection:** We retrieve detection and photometric catalogs from PostgreSQL database tables. Using SQL scripts, we select objects meeting the following criteria of (i) magnitude and color selections and (ii) *hscPipe* parameters and flags.

- (i) **Magnitude and color selection:** To identify objects with an NB magnitude excess in the HSC catalog, we apply the magnitude and color selection criteria:

$$\begin{aligned}
 &NB921 \leq NB921_{5\sigma} \ \&\& \ z - NB921 \geq 1.0 \\
 &\ \&\& \ g > g_{3\sigma} \ \&\& \ r > r_{3\sigma} \\
 &\ \&\& \ [(z \leq z_{3\sigma} \ \&\& \ i - z \geq 1.3) \ \text{or} \ z > z_{3\sigma}] \\
 &\ \text{for } z \sim 6.6,
 \end{aligned}$$

and,

$$\begin{aligned}
 &NB816 \leq NB816_{5\sigma} \ \&\& \ i - NB816 \geq 1.2 \\
 &\ \&\& \ g > g_{3\sigma} \\
 &\ \&\& \ [(r \leq r_{3\sigma} \ \&\& \ r - i \geq 1.0) \ \text{or} \ r > r_{3\sigma}] \\
 &\ \text{for } z \sim 5.7,
 \end{aligned}$$

where the subscripts  $5\sigma$  and  $3\sigma$  indicate the  $5\sigma$  and  $3\sigma$  magnitude limits for a given filter, respectively. These

**Table 1.** Properties of the HSC SSP S16A NB Data

Field	R.A. (J2000)	Dec. (J2000)	Area (deg <sup>2</sup> )	$T_{\text{exp}}$ (hour)	$m_{\text{lim}}(5\sigma, 1.5''\phi)$ (mag)	$N_{\text{LAE,ALL}}$	$N_{\text{LAE,F}}$
(1)	(2)	(3)	(4)	(5)	(6)	(7)	(8)
<i>NB921 (<math>z \simeq 6.6</math>)</i>							
UD-COSMOS	10:00:28	+02:12:21	2.04667	11.25	25.6	435	161
UD-SXDS	02:18:00	−05:00:00	2.01667	7.25	25.5	60	24
D-COSMOS	10:00:60	+02:13:53	5.30528	2.75	25.3	249	51
D-DEEP23	23:30:22	−00:44:38	5.76111	1.00	24.9	178	38
D-ELAISN1	16:10:00	+54:17:51	6.08111	1.75	25.3	351	47
<b>Total</b>	—	—	21.2108	24.00	—	1273	321
<i>NB816 (<math>z \simeq 5.7</math>)</i>							
UD-COSMOS	10:00:28	+02:12:21	1.96861	5.50	25.7	202	176
UD-SXDS	02:18:00	−05:00:00	1.92806	3.75	25.5	224	189
D-DEEP23	23:30:22	−00:44:38	4.37139	1.00	25.2	423	283
D-ELAISN1	16:10:00	+54:17:51	5.55500	1.00	25.3	232	132
<b>Total</b>	—	—	13.8231	11.25	—	1081	780

(1) Field.

(2) Right ascension.

(3) Declination.

(4) Survey area with the HSC SQL parameters in Table 2.

(5) Total exposure time of the NB imaging observation.

(6) Limiting magnitude of the NB image defined by a  $5\sigma$  sky noise in a  $1.''5$  diameter circular aperture.

(7) Number of the LAE candidates in the ALL (unforced+forced) catalog.

(8) Number of the LAE candidates in the forced catalog.

**Table 2.** HSC SQL Parameters and Flags for Our LAE Selection

Parameter or Flag	Value	Band	Comment
detect_is_tract_inner	True	—	Object is in an inner region of a tract and not in the overlapping region with adjacent tracts
detect_is_patch_inner	True	—	Object is in an inner region of a patch and not in the overlapping region with adjacent patches
countinputs	$\geq 3$	<i>NB</i>	Number of visits at a source position for a given filter.
flags_pixel_edge	False	<i>grizy, NB</i>	Locate within images
flags_pixel_interpolated_center	False	<i>grizy, NB</i>	None of the central $3 \times 3$ pixels of an object is interpolated
flags_pixel_saturated_center	False	<i>grizy, NB</i>	None of the central $3 \times 3$ pixels of an object is saturated
flags_pixel_cr_center	False	<i>grizy, NB</i>	None of the central $3 \times 3$ pixels of an object is masked as cosmic ray
flags_pixel_bad	False	<i>grizy, NB</i>	None of the pixels in the footprint of an object is labelled as bad

magnitude and color selection criteria are similar to those of e.g., Ouchi et al. 2008; Ouchi et al. 2010. The  $\text{Ly}\alpha$  EW limit of our LAE selection is  $\simeq 20 \text{ \AA}$  (see Konno et al. 2017).

- (ii) **Parameters and Flags:** Similar to Ono et al. (2017), we set several hscPipe parameters and flags in the HSC catalog to exclude e.g., blended sources, and objects affected by saturated pixels, and nearby bright source halos. We also mask regions where exposure times are relatively short by using the countinputs parameter,  $N_c$ , which denotes the number of exposures at a source posi-

tion for a given filter. Table 2 summarizes the values and brief explanations of the hscPipe parameters and flags used for our LAE selection. The full details of these parameters and flags are presented in Aihara et al. (2017a). To search for LAEs in large areas of the HSC fields, we do not apply the countinputs parameter to the BB images.

The number of objects selected in this process is  $n_{\text{SQL}} \simeq 100,000$ .

- (2) **Visual inspections for object images:** To exclude cosmic rays, cross-talks, compact stellar objects, and artificial

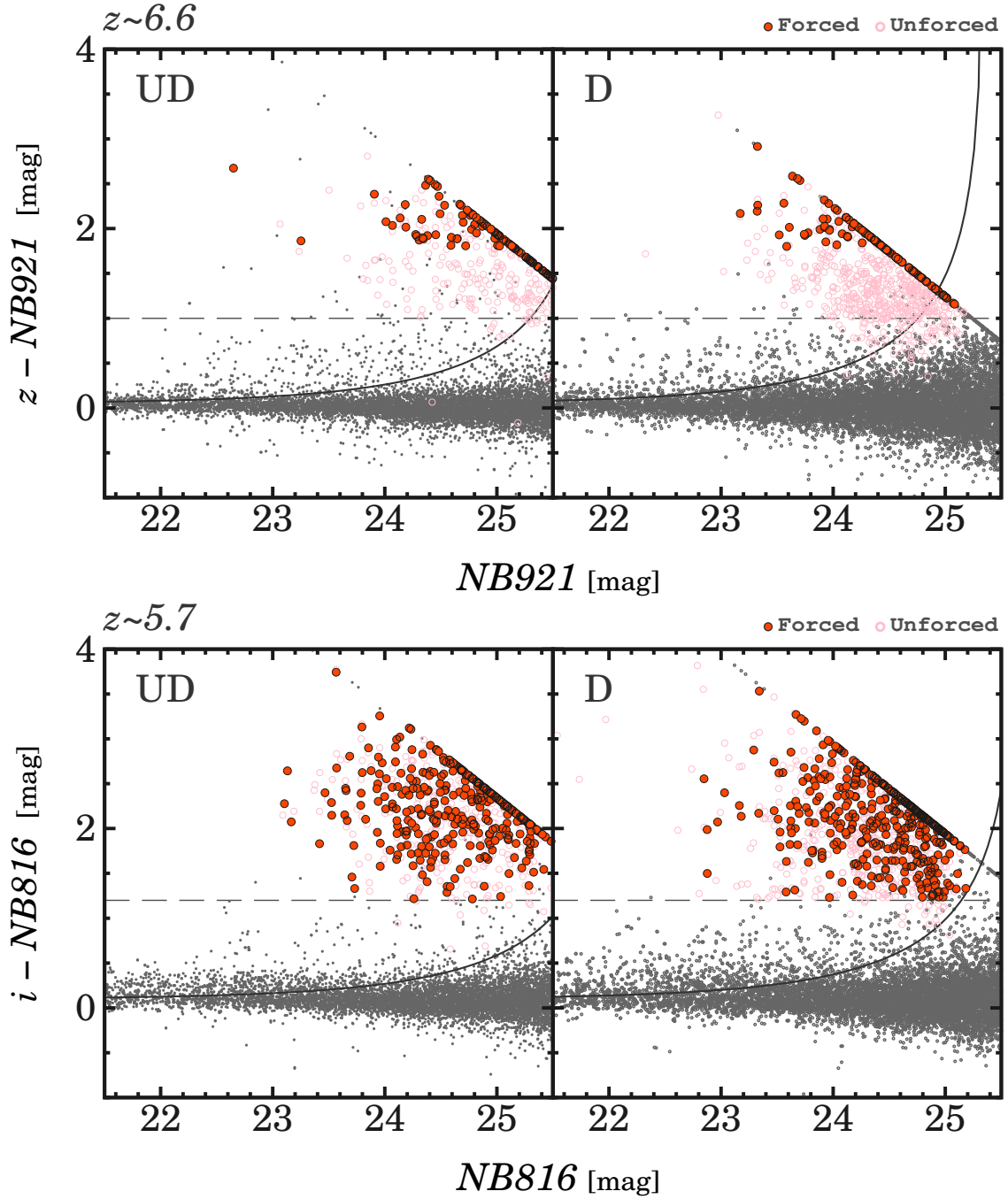


**Fig. 3.** (Top)  $z - \text{NB921}$  as a function of  $\text{NB921}$  magnitude for the LAEs at  $z \simeq 6.6$ . The filled red and open magenta circles denote the LAEs in the forced and unforced catalogs, respectively. For the LAEs undetected in the  $z$ -band images, the  $z$ -band magnitudes are replaced with the  $2\sigma$  magnitude limits. The gray dots present detected objects in the  $\text{NB921}$  images. The curve shows the  $3\sigma$  error track of  $z - \text{NB921}$  color defined by Equation 1. The  $3\sigma$  error track is derived by using typical values of BB and NB limiting magnitudes for the UD and D fields. The x-axis value is the  $\text{BB} - \text{NB}$  color calculated from forced magnitudes. (Bottom)  $i - \text{NB816}$  color as a function of  $\text{NB816}$  magnitude for the LAEs at  $z \simeq 5.7$ .

diffuse objects, we perform visual inspections for the BB and NB images of all the objects selected in the process (1). For the reliability check, four authors in this paper have individually carried out such visual inspections for the UD-COSMOS fields, and compare the results of the LAE selection. We do not find a large difference of our visual inspection

results. The number of objects selected in this process is  $n_{\text{vis}} \simeq 10,000$ .

- (3) **Rejection of variable and moving objects with multi-epoch images:** We exclude variable and moving objects such as supernovae, AGNs, satellite trails, and asteroids using multi-epoch NB images. The NB images were typically

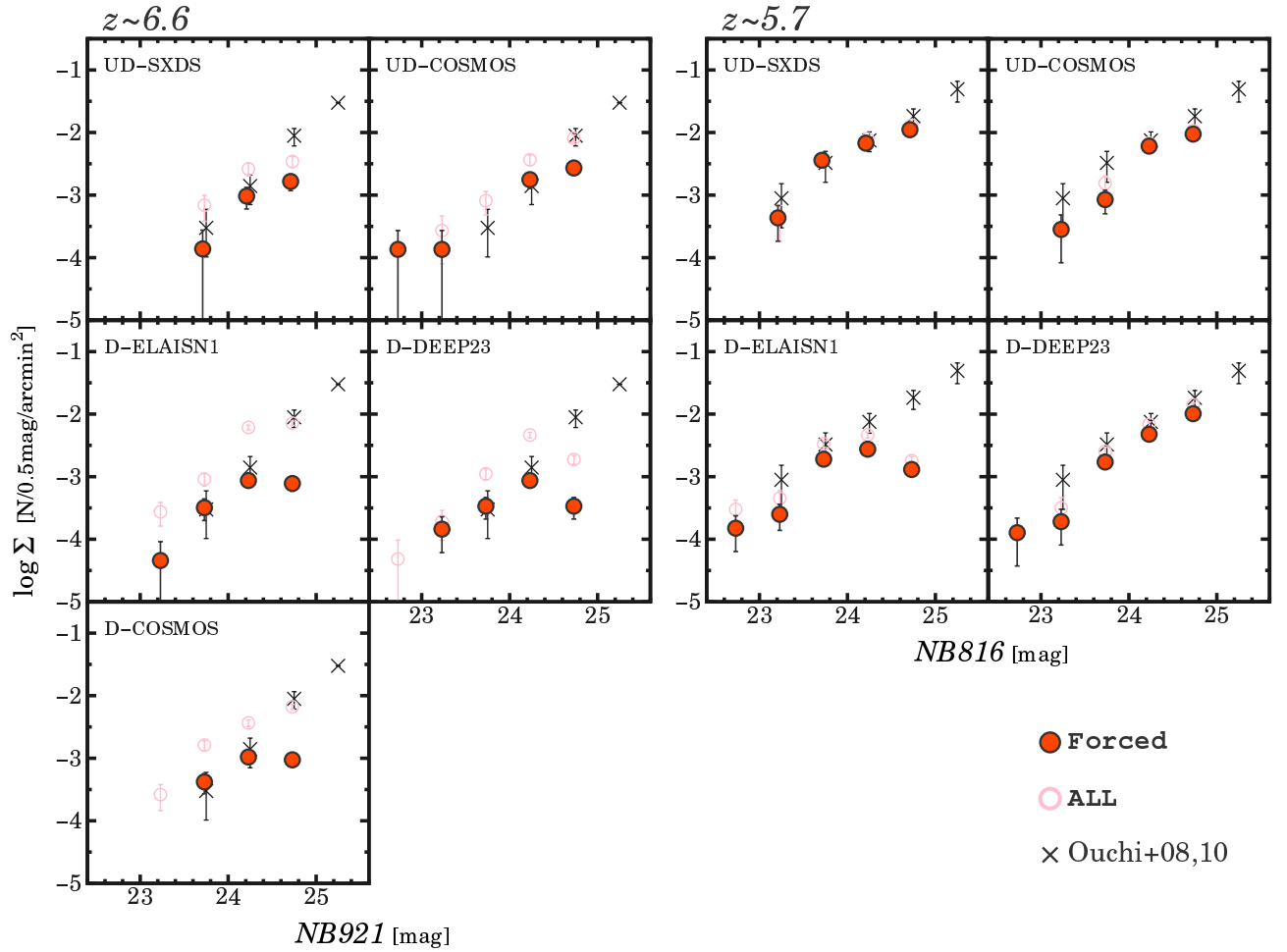


**Fig. 4.** Surface number density (SND) of the HSC LAEs at  $z \simeq 6.6$  (five panels at the left) and  $\simeq 5.7$  (four panels at the right) in each UD and D field. The filled red and open magenta circles indicate the LAEs in the *forced* and *ALL* catalog, respectively. The error bars are given by Poisson statistics from the number of LAEs. The gray crosses represent the LAEs in Ouchi et al. (2010) for  $z \simeq 6.6$  and Ouchi et al. (2008) for  $z \simeq 5.7$ . The SND slight declines in the HSC LAEs at  $NB \gtrsim 24.5$  mag would be originated from the incompleteness of the LAE detection and selection. The completeness-corrected SNDs are presented in Konno et al. (2017). The data points of the HSC LAEs are slightly shifted along x-axis for clarity.

taken a few months - years after the BB imaging observations. For this reason, there is a possibility that sources with an NB flux excess are variable or moving objects which happened to enhance the luminosities during the NB imaging observations.

The NB images are created by coadding  $\simeq 10 - 20$  and  $\simeq 3 - 5$  frames of 15 minute exposures for the current HSC UD and D data, respectively. Using the multi-epoch images, we automatically remove the variable and moving objects as follows. First, we measure the flux for individual epoch images,  $f_{\text{epoch}}$ , for each object. Next, we obtain an average,  $f_{\text{ave}}$ , and a standard deviation,  $\sigma_{\text{epoch}}$ , from a set of the  $f_{\text{epoch}}$  values after a  $2\sigma$  flux clipping. Finally, we discard an object having at least a multi-epoch image with a significantly large  $f_{\text{epoch}}$  value of  $f_{\text{epoch}} \geq f_{\text{ave}} + A_{\text{epoch}} \times \sigma_{\text{epoch}}$ . Here we tune the  $A_{\text{epoch}}$  factor based on the depth of the NB fields. The  $A_{\text{epoch}}$  value is typically  $\simeq 2.0 - 2.5$ . Figure 2 shows

examples of the spurious sources.

We also perform visual inspections for multi-epoch images to remove contaminants which are not excluded in the automatic rejection above. We refer the remaining objects after this process as the LAE *ALL* catalog.

#### (4) Forced selection:

We select LAEs meeting only the selection criteria of forced  $BB - NB$  colors. These LAEs are similar to objects selected in the double-image mode of SExtractor. Here we also adopt a new color criterion of  $z - NB921 > 1.8$  for  $z \simeq 6.6$  LAEs for the consistency of the Ly $\alpha$  EW limits between our HSC and previous LAE studies (see Konno et al. 2017 for more details). Moreover, we also remove the objects in masked regions defined by the `flags_pixel_bright_object_[center/any]` parameters. We refer the set of the remaining objects after this process as the forced LAE catalog. This forced LAE cata-



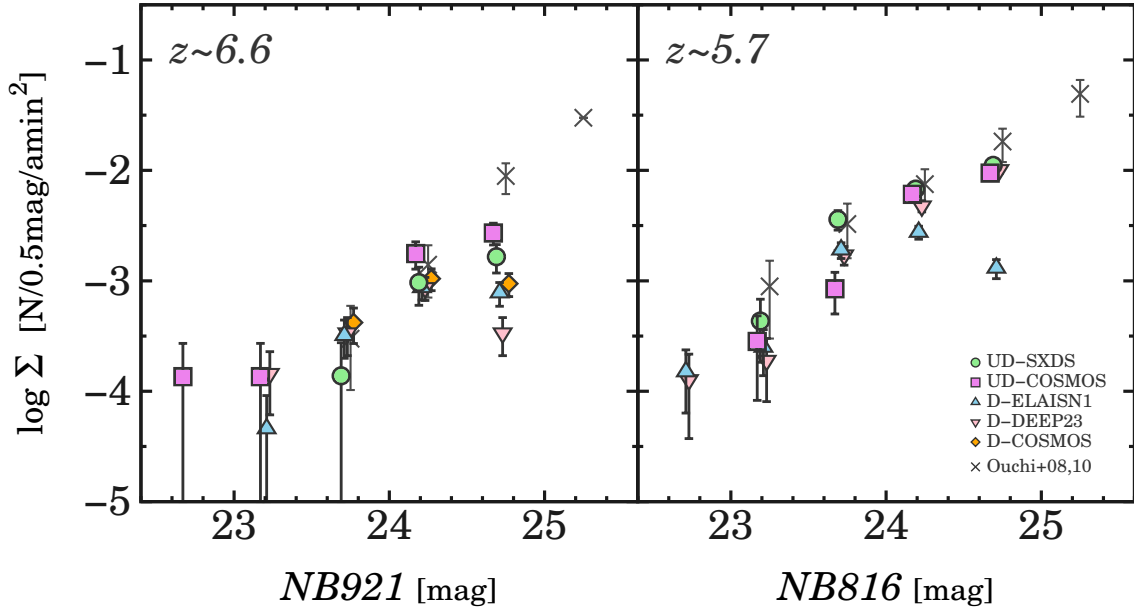


**Fig. 5.** Surface number density (SND) as a function of NB magnitude for the LAEs at  $z \sim 6.6$  (left) and  $\sim 5.7$  (right) in the forced catalog. The colored symbols denote the LAEs in each UD and D field (green circles: UD-SXDS; magenta squares: UD-COSMOS; cyan triangles: D-ELAISN1; light-red inverse-triangles: D-DEEP23; orange diamonds: D-COSMOS). The error bars are given by Poisson statistics from the number of LAEs. The gray crosses represent the LAEs in Ouchi et al. (2010) for  $z \sim 6.6$  and Ouchi et al. (2008) for  $z \sim 5.7$ . The SND slight declines in of the HSC LAEs at  $NB \gtrsim 24.5$  mag would be originated from the incompleteness of the LAE detection and selection. The completeness-corrected SNDs are presented in Konno et al. (2017). The data points of the HSC LAEs are slightly shifted along x-axis for clarity.

**Table 3.** Catalog of the HSC LAE candidates.

Object ID	$\alpha$ (J2000)	$\delta$ (J2000)	$NB_{\text{tot}}$ (mag)	$g_{\text{tot}}$ (mag)	$r_{\text{tot}}$ (mag)	$i_{\text{tot}}$ (mag)	$z_{\text{tot}}$ (mag)	$y_{\text{tot}}$ (mag)	Flag
(1)	(2)	(3)	(4)	(5)	(6)	(7)	(8)	(9)	(10)
HSC J021601–041442	02:16:01.18	−04:14:42.74	26.89	27.03	26.65	25.28	25.29	23.85	0
HSC J021609–050236	02:16:09.74	−05:02:36.02	27.53	27.29	27.04	26.32	28.73	24.89	0
HSC J021638–043228	02:16:38.19	−04:32:28.42	28.20	27.84	27.55	26.17	29.77	24.74	0
HSC J021702–050604	02:17:02.56	−05:06:04.61	30.81	27.58	33.43	26.53	26.35	24.64	1
HSC J021754–051454	02:17:54.17	−05:14:54.50	28.98	27.59	28.21	26.09	25.21	24.01	1

(1) Object ID.

(2) Right ascension.

(3) Declination.

(4)–(9) Total magnitude of  $g$ -,  $r$ -,  $i$ -,  $z$ ,  $y$ , and  $NB$ -bands.

(10) Flag. If the value is 1, the LAE candidate is selected in the forced selection criteria.

(The complete table is available in a machine-readable form in the online journal.)

log is used for studies on LAE statistics such as measurements of  $\text{Ly}\alpha$  EW scale lengths. Note that we do not apply the `flags.pixel.bright_object.[center/any]` masking to the LAE ALL catalog in order to maximize LAE targets for spectroscopic follow-up observations.

In total, we identify 2,354 and 1,101 LAE candidates in the ALL and forced catalogs, respectively. Table 1 presents the numbers of LAE candidates. The LAE candidates selected only in the unforced and forced selection criteria are referred to as the unforced and forced LAEs, respectively. The examples of unforced and forced LAEs are shown in Figure 2. Table 3

presents the machine-readable catalog of the LAE candidates.

Figure 3 shows the color-magnitude diagrams for the LAE candidates. The solid curves in the color magnitude diagrams indicate the  $3\sigma$  errors of  $BB - NB$  color as a function of the NB flux,  $f_{NB}$ , given by

$$\pm 3\sigma_{BB-NB} = -2.5 \log_{10} \left( 1 \mp 3 \frac{\sqrt{f_{1\sigma NB}^2 + f_{1\sigma BB}^2}}{f_{NB}} \right), \quad (1)$$

where  $f_{1\sigma NB}$  and  $f_{1\sigma BB}$  are the  $1\sigma$  flux error in the  $z$  and  $NB921$  ( $i$  and  $NB816$ ) bands for  $z \sim 6.6$  ( $z \sim 5.7$ ), respectively. As shown in Figure 3, the LAE candidates have a significant NB magnitude excess. There are unforced LAE candi-

dates with a  $BB - NB$  color below the  $3\sigma$  error tracks defined by Equation 1. Such unforced LAE candidates are selected due to an NB magnitude excess in unforced  $BB - NB$  colors.

## 4 Checking the Reliability of Our LAE Selection

Here we check the reliability of our LAE selection.

### 4.1 Spectroscopic Confirmations

We have conducted optical spectroscopic observations for bright LAE candidates with  $NB \lesssim 24$  mag, and have confirmed 21 LAEs. In addition, we find that 76 LAEs are spectroscopically confirmed by previous studies for the SXDS and COSMOS fields (Murayama et al. 2007; Ouchi et al. 2008; Taniguchi et al. 2009; Ouchi et al. 2010; Mallery et al. 2012; Sobral et al. 2015; Higuchi et al. in preparation). In total, 97 LAEs have been confirmed in our spectroscopy and previous studies. The details of the spectroscopic observations and contamination rates are given by Shibuya et al. (2017b).

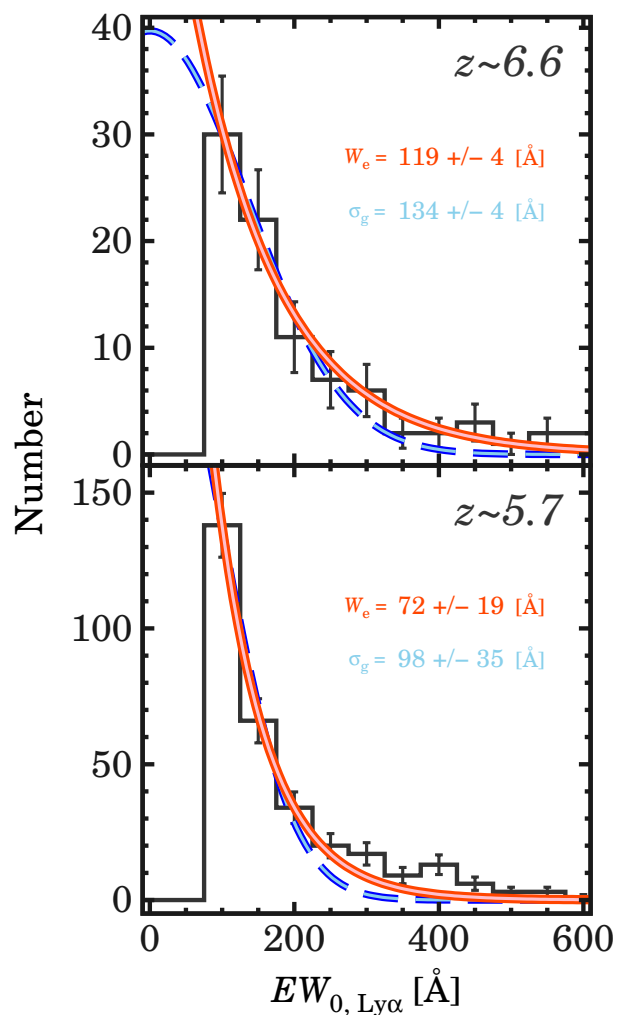
### 4.2 LAE Surface Number Density

Figure 4 shows the surface number density (SND) of our LAE candidates and LAEs identified in previous Subaru/SCam NB surveys, SCam LAEs (e.g., Ouchi et al. 2008; Ouchi et al. 2010). We find that the SNDs of the forced LAEs are comparable to those of SCam LAEs. We also identify SND humps of our LAEs at  $z \simeq 6.6$  at the bright-end of  $NB \simeq 23$  mag in UD-COSMOS. The presence of such a SND hump has been reported by  $z \simeq 6.6$  LAE studies (e.g., Matthee et al. 2015). The slight declines in SNDs at a faint NB magnitude of  $NB \gtrsim 24.5$  mag would be originated from the incompleteness of the LAE detection and selection. Konno et al. (2017) present the SND corrected for the incompleteness.

Figure 5 compiles the SNDs of all the HSC UD and D fields. We find that our SNDs show a small field-to-field variation, but typically follow those of SCam LAEs.

### 4.3 Matching Rate of HSC LAEs and SCam LAEs

The UD fields have been observed previously by SCam equipped with the  $NB921$  and  $NB816$  filters (e.g., Ouchi et al. 2008; Ouchi et al. 2010). We compare the catalogs of our selected HSC LAE candidates and SCam LAEs, and calculate the object matching rates as a function of NB magnitudes. The object matching rate between the HSC LAEs and SCam LAEs is  $\simeq 90\%$  at a bright NB magnitudes of  $\lesssim 24$  mag. The high object matching rate indicates that we adequately identify LAEs in our selection processes. However, the matching rate decreases to  $\simeq 70\%$  at a faint magnitude of  $\simeq 24.5$  mag. This is due to



**Fig. 6.**  $\text{Ly}\alpha$  EW distribution for the HSC LAEs at  $z \simeq 6.6$  (top) and  $z \simeq 5.7$  (bottom). The black histograms indicate the forced LAEs. The error bars are given by Poisson statistics from the number of sample LAEs. The red solid and blue dashed lines present the best-fit exponential and Gaussian functions of Equations 3 and 4, respectively.

the shallow depth of the HSC NB fields compared to the SCam ones. Konno et al. (2017) discuss the detection completeness of faint LAEs.

## 5 Results

Here we present the  $\text{Ly}\alpha$  EW distributions (Section 5.1) and LABs selected with the HSC data (Section 5.2). For the consistency with previous LAE studies, we use the forced LAE sample in the following analyses.

### 5.1 $\text{Ly}\alpha$ EW Distribution

We present the  $\text{Ly}\alpha$  EW distributions for LAEs at  $z \simeq 5.7 - 6.6$ . To obtain the  $\text{Ly}\alpha$  EW for each LAE, we assume that both of NB and BB filters have top-hat response functions. The  $\text{Ly}\alpha$

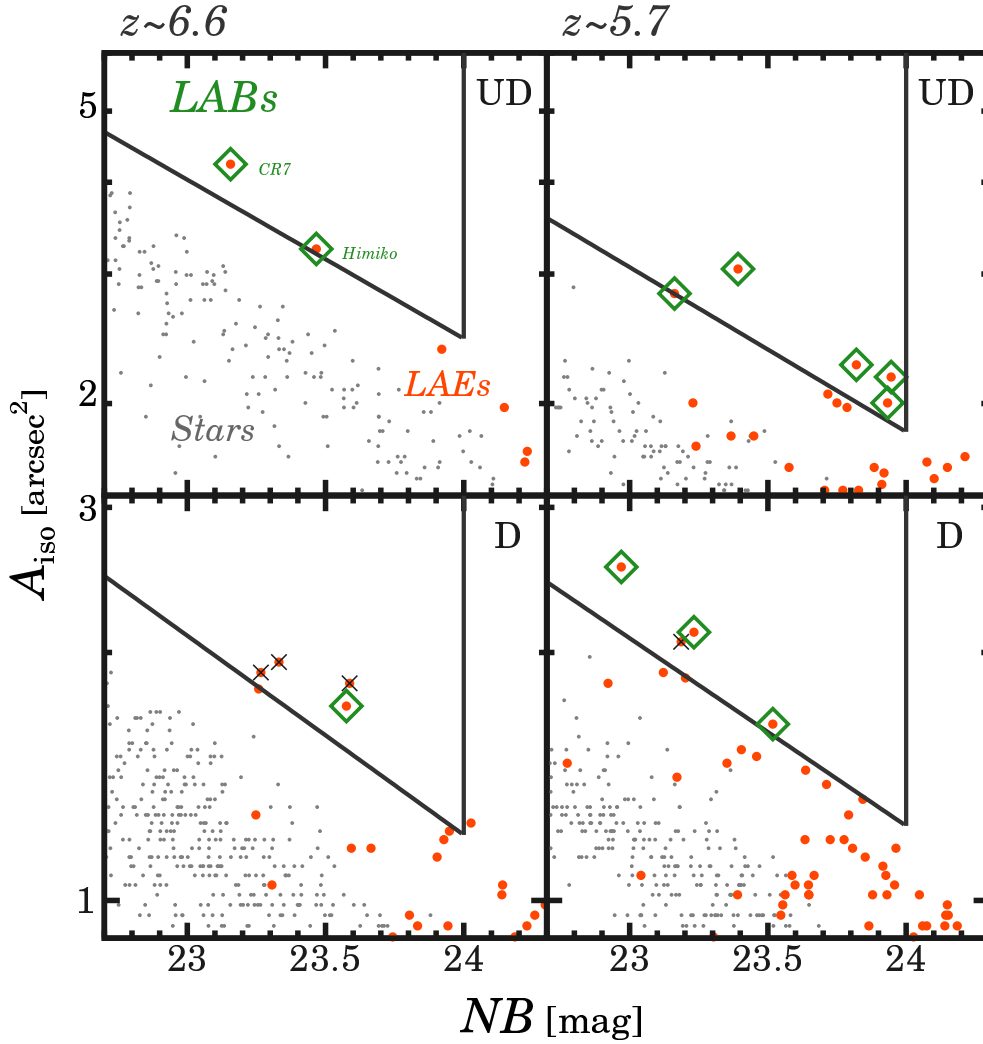


**Fig. 7.** Isophotal area,  $A_{\text{iso}}$ , as a function of NB magnitude to select LABs at  $z \simeq 6.6$  (left) and  $z \simeq 5.7$  (right). The top and bottom panels show the UD and D fields, respectively. The green diamonds denote the LABs. The filled red circles indicate the LAEs in the forced catalog. The gray dots represent star-like point sources selected in the HSC NB images. The diagonal and vertical lines denote the LAB selection criteria of  $A_{\text{iso}}$  and NB magnitude. The diagonal lines are defined by the  $2.5\sigma$  deviation from the  $A_{\text{iso}}$ -NB magnitude distribution for the star-like point sources. The filled red circles with a cross indicate unreliable LAB candidates which are affected by e.g., diffuse halos of nearby bright stars. The  $z \simeq 6.6$  LABs in the UD fields are CR7 (Sobral et al. 2015) and Himiko (Ouchi et al. 2009).

EW is calculated by using an equation of

$$EW_{0,\text{Ly}\alpha} = \frac{(f_{\text{NB}} - f_{\text{BB}}) \Delta\lambda_{\text{NB}} \Delta\lambda_{\text{BB}}}{\Delta\lambda_{\text{BB}} f_{\text{BB}} - \Delta\lambda_{\text{NB}} f_{\text{NB}}} \frac{1}{1 + z_{\text{Ly}\alpha}}, \quad (2)$$

where  $f$  is the flux density per unit wavelength,  $\Delta\lambda$  is the width of a given filter,  $z_{\text{Ly}\alpha}$  is the redshift of  $\text{Ly}\alpha$  emission line (e.g., Nakajima et al. 2012). The subscripts  $\text{NB}$  and  $\text{BB}$  indicate  $\text{NB}921$  and  $y$  ( $\text{NB}816$  and  $z$ ) images for  $z \simeq 6.6$  ( $z \simeq 5.7$ ) LAEs. Note that the  $y$  and  $z$ -band magnitudes trace the UV continuum emission without  $\text{Ly}\alpha$  flux contaminations to these BB filter responses. In the HSC LAE sample, we identify  $\sim 700$  LAEs with a LEW of  $\gtrsim 240 \text{ \AA}$  that are candidates of young-metal poor galaxies and AGNs. The fraction of the LEW LAEs to all LAEs is moderately large,  $\sim 30\%$ .

We evaluate the  $\text{Ly}\alpha$  EW distributions. We fit the exponen-

tial and Gaussian functions to the  $\text{Ly}\alpha$  EW distributions (e.g., Gronwall et al. 2007; Kashikawa et al. 2011; Oyarzún et al. 2016). The exponential and Gaussian functions are described by equations of

$$\frac{dN}{dEW} = N \exp\left(-\frac{EW^2}{W_e}\right), \quad (3)$$

and,

$$\frac{dN}{dEW} = N \frac{1}{\sqrt{2\pi}\sigma_g^2} \exp\left(-\frac{EW^2}{2\sigma_g^2}\right), \quad (4)$$

respectively. Here  $N$  is the galaxy number,  $W_e$  and  $\sigma_g$  are the  $\text{Ly}\alpha$  EW scale lengths of the exponential and Gaussian functions, respectively.

Figure 6 shows the observed and best-fit  $\text{Ly}\alpha$  EW distributions. We obtain the best-fit  $\text{Ly}\alpha$  scale lengths of  $W_e = 119 \pm 4$

**Table 4.** Properties of the LABs selected in the HSC NB Data.

Object ID	$\alpha$ (J2000)	$\delta$ (J2000)	$NB_{\text{tot}}$	$UV_{\text{tot}}$	$\log L_{\text{Ly}\alpha}$	$EW_{0,\text{Ly}\alpha}$	$z_{\text{spec}}$
(1)	(2)	(3)	(mag)	(mag)	( $\text{erg s}^{-1}$ )	( $\text{\AA}$ )	(8)
<i>NB921</i> ( $z \simeq 6.6$ )							
HSC J100058+014815 <sup>a</sup>	10:00:58.00	+01:48:15.14	23.25	24.48	43.9 <sup>e</sup>	211 <sup>e</sup>	6.604 <sup>a</sup>
HSC J021757–050844 <sup>b</sup>	02:17:57.58	–05:08:44.64	23.50	25.40	43.4 <sup>e</sup>	78 <sup>e</sup>	6.595 <sup>b</sup>
HSC J100334+024546 <sup>c</sup>	10:03:34.66	+02:45:46.56	23.61	24.97	43.5 <sup>e</sup>	61.1 <sup>e</sup>	6.575 <sup>c</sup>
<i>NB816</i> ( $z \simeq 5.7$ )							
HSC J100129+014929	10:01:29.07	+01:49:29.81	23.47	25.87	43.3 <sup>e</sup>	60.9 <sup>e</sup>	5.707 <sup>d</sup>
HSC J100109+021513	10:01:09.72	+02:15:13.45	23.13	25.77	43.4 <sup>e</sup>	19.7 <sup>e</sup>	5.712 <sup>d</sup>
HSC J100123+015600	10:01:23.84	+01:56:00.46	23.94	26.43	43.1 <sup>e</sup>	11.4 <sup>e</sup>	5.726 <sup>d</sup>
HSC J095946+013208	09:59:46.73	+01:32:08.45	24.16	26.12	43.0	27.9	—
HSC J100139+015428	10:01:39.94	+01:54:28.34	24.11	26.58	43.1	78.5	—
HSC J161927+551144	16:19:27.73	+55:11:44.70	22.88	24.86	43.6	71.4	—
HSC J161403+535701	16:14:03.82	+53:57:01.25	23.53	25.32	43.2	20.6	—
HSC J232924+003600	23:29:24.85	+00:36:00.34	23.62	26.48	43.2	28.6	—

(1) Object ID.

(2) Right ascension.

(3) Declination.

(4) Total magnitudes of *NB921*- and *NB816*-bands for  $z \simeq 6.6$  and  $z \simeq 5.7$ , respectively.(5) Total magnitudes of *y*- and *z*-bands for  $z \simeq 6.6$  and  $z \simeq 5.7$ , respectively.(6)  $\text{Ly}\alpha$  luminosity.(7) Rest-frame equivalent width of  $\text{Ly}\alpha$  emission line.

(8) Spectroscopic redshift.

<sup>a</sup> CR7 in Sobral et al. (2015).<sup>b</sup> Himiko in Ouchi et al. (2009).<sup>c</sup> Spectroscopically confirmed in Shibuya et al. (2017b).<sup>d</sup> Spectroscopically confirmed in Mallery et al. (2012).<sup>e</sup> Spectroscopic measurements.

( $72 \pm 19$ )  $\text{\AA}$  and  $\sigma_g = 134 \pm 4$  ( $98 \pm 35$ )  $\text{\AA}$  for  $z \simeq 6.6$  ( $z \simeq 5.7$ ) LAEs, as summarized in Table 5. We find that the  $\text{Ly}\alpha$  EW distributions are reasonably explained by the exponential profiles instead of the Gaussian functions. In Section 6.1, we discuss the redshift evolution of the  $\text{Ly}\alpha$  EW scale lengths.

## 5.2 LABs at $z \simeq 5.7 - 6.6$

We search for LABs with spatially-extended  $\text{Ly}\alpha$  emission. To identify LABs, we measure the NB isophotal areas,  $A_{\text{iso}}$ , for the forced LAEs. In this process, we include an unforced LAE, Himiko, which is an LAB identified in a previous SCam NB survey (Ouchi et al. 2009). First, we estimate the sky background level of the NB cutout images. Next, we run the *SExtractor* with the sky background level, and obtain the  $A_{\text{iso}}$  values as pixels with fluxes brighter than the  $2\sigma$  sky fluctuation. Note that the NB magnitudes include both fluxes of  $\text{Ly}\alpha$  and the rest-frame UV continuum emission. Instead of creating  $\text{Ly}\alpha$  images by subtracting the flux contribution of the rest-frame UV continuum emission, we here simply use the NB images for consis-

tency with previous studies (e.g., Ouchi et al. 2009).

Using  $A_{\text{iso}}$  and NB magnitude diagrams, we select LABs which are significantly extended compared to point sources. This selection is similar to that of Yang et al. (2010). Figure 7 presents  $A_{\text{iso}}$  as a function of total *NB* magnitude. We also plot star-like point sources which are randomly selected in HSC NB fields. The  $A_{\text{iso}}$  and NB magnitude selection window is defined by the  $2.5\sigma$  deviation from the  $A_{\text{iso}}$ -NB magnitude distribution for the star-like point sources. We perform visual inspections for the NB cutout images to remove unreliable LABs which are significantly affected by e.g., diffuse halos of nearby bright stars.

In total, we identify 11 LABs at  $z \simeq 5.7 - 6.6$ . Figure 8 and Table 4 present multi-band cutout images and properties for the LABs, respectively. Our HSC LAB selection confirms that CR7 and Himiko have a spatially extended  $\text{Ly}\alpha$  emission. Six out of our 11 LABs have been confirmed by our spectroscopic follow-up observations (Shibuya et al. 2017b) and previous studies (Ouchi et al. 2009; Mallery et al. 2012; Sobral et al. 2015). In Section 6.2, we discuss the redshift evolution of the

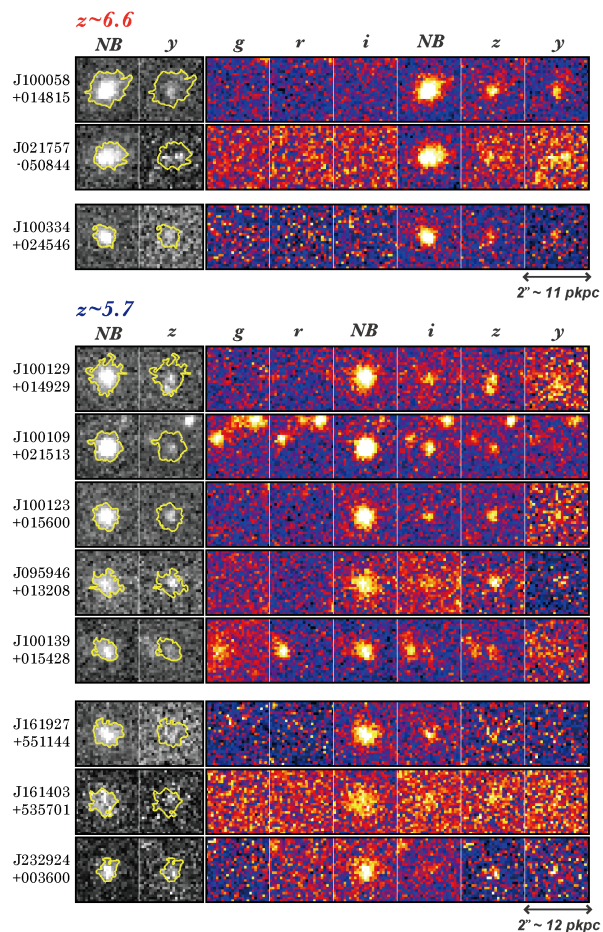


**Fig. 8.** Postage stamps of the LABs selected with the HSC NB data. The yellow contours indicate isophotal apertures with a threshold of  $2\sigma$  sky background noise level. The size of the cutout images is  $2'' \times 2''$ .

LAB number density.

## 6 Discussion

### 6.1 Redshift Evolution of Ly $\alpha$ EW Distribution

We discuss the redshift evolution of the Ly $\alpha$  EW scale lengths in a compilation of the results from literature (Zheng et al. 2014; Ouchi et al. 2008; Nilsson et al. 2009; Hu et al. 2010; Kashikawa et al. 2011; Cowie et al. 2011; Ciardullo et al. 2012). Figure 9 shows the redshift evolution of the Ly $\alpha$  EW scale lengths at  $z \simeq 0 - 7$ . Zheng et al. (2014) have identified the  $(1+z)$ -form of the Ly $\alpha$  EW scale length evolutions. We find that our best-fit Ly $\alpha$  EW scale lengths are roughly comparable to Zheng et al.'s  $(1+z)$ -form evolutions. The large HSC LAE sample confirms the redshift evolution of Ly $\alpha$  EW scale lengths from  $z \simeq 0$  to  $\simeq 7$  with small uncertainties. This indicates that galaxies with a large Ly $\alpha$  EW might be more common at  $z \simeq 6 - 7$  than  $z \simeq 0 - 5$ . However, the Ly $\alpha$  EW scale length measurements would largely depend on BB and NB depths and Ly $\alpha$  EW cuts. To discuss the redshift evolution of Ly $\alpha$  scale

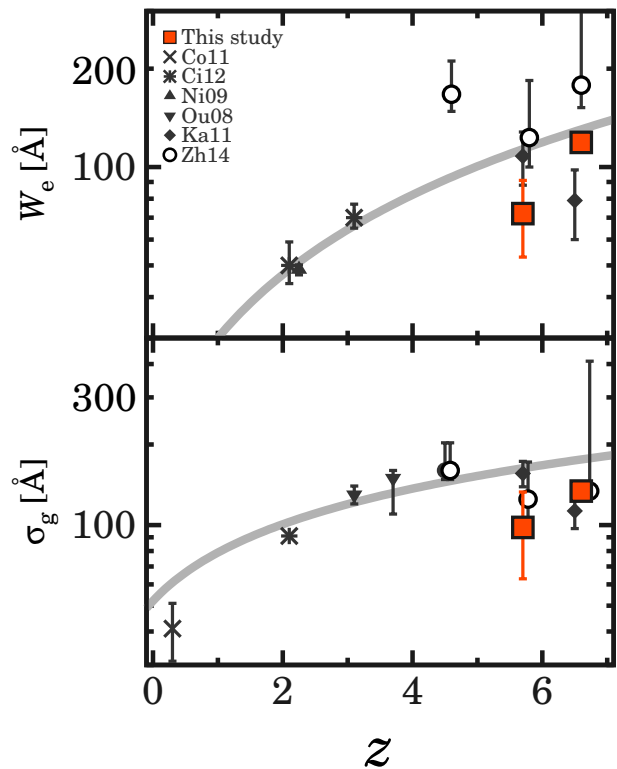


**Fig. 9.** Redshift evolution of the best-fit Ly $\alpha$  EW scale lengths of the exponential (top) and Gaussian (bottom) functions. The red squares indicate our HSC LAEs. The black symbols are taken from the data points in literature which have been compiled in Zheng et al. (2014) (cross: Cowie et al. 2011; asterisks: Ciardullo et al. 2012; filled triangle: Nilsson et al. 2009; filled inverse triangles: Ouchi et al. 2008; filled diamonds: Kashikawa et al. 2011; open circles: results of Monte-Carlo simulations using data of Zheng et al. 2014 and Hu et al. 2010). The gray curves indicate the best-fit  $(1+z)$ -form functions obtained in Zheng et al. (2014).

lengths accurately at  $z \simeq 0 - 7$ , we have to use BB and NB depths and Ly $\alpha$  EW limits which are the same as those of previous studies.

### 6.2 Redshift Evolution of LAB Number Density

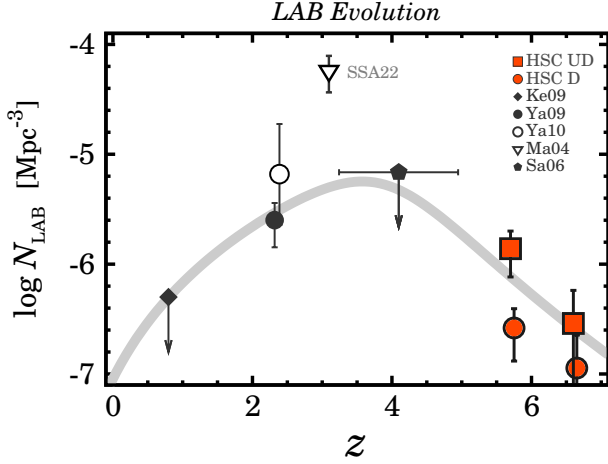
We discuss the redshift evolution of the LAB number density,  $N_{\text{LAB}}$ , in a compilation of LABs from literature (Keel et al. 2009; Yang et al. 2009; Yang et al. 2010; Matsuda et al. 2009; Saito et al. 2006). Figure 10 shows the number density for LABs at  $z \simeq 0 - 7$ . All the  $N_{\text{LAB}}$  values are obtained from LABs identified down to the NB surface brightness limit of  $\simeq 5 \times 10^{-18} \text{ erg s}^{-1} \text{ cm}^{-2} \text{ arcsec}^{-2}$  (Yang et al. 2010). We identify an evolutionary trend that  $N_{\text{LAB}}$  increases from  $z \simeq 7$  to  $\simeq 3$  and subsequently decreases from  $z \simeq 3$  to  $\simeq 0$ . This trend of the LAB number density evolution is similar to the Madau-Lilly plot of the cosmic SFR density (SFRD) evolution (e.g., Madau et al. 1996; Lilly et al. 1996). The number density of the LABs at  $z \simeq 6 - 7$  is  $\simeq 10^{-7} - 10^{-6} \text{ Mpc}^{-3}$  that is  $\simeq 10 - 100$  times lower than those claimed for LABs at  $z \simeq 2 - 3$  (e.g., Matsuda



**Table 5.** Best-fit Ly $\alpha$  EW Scale Lengths

Redshift	$W_e$ ( $\text{\AA}$ )	$\sigma_g$ ( $\text{\AA}$ )
(1)	(2)	(3)
6.6	$119 \pm 4$	$134 \pm 4$
5.7	$72 \pm 19$	$98 \pm 35$

(1) Redshift.

(2) Best-fit Ly $\alpha$  EW scale length of the exponential form.(3) Best-fit Ly $\alpha$  EW scale length of the Gaussian form.

**Fig. 10.** Redshift evolution of the LAB number density. The filled red squares and filled red circles denote the LABs selected in the HSC UD and D fields, respectively. The error bars are given by Poisson statistics from the LAB number counts. The black symbols show LABs in the literature (filled diamond: Keel et al. 2009; filled circle: Yang et al. 2009; open circle: Yang et al. 2010; filled inverse-triangle: Matsuda et al. 2004; pentagon: Saito et al. 2006). All the measurements are based on LABs identified down to the surface brightness limit of  $\simeq 5 \times 10^{-18} \text{ erg s}^{-1} \text{ cm}^{-2} \text{ arcsec}^{-2}$ . The gray solid curve represents the best-fit formula of Equation 5 to the data points except for the measurement in the SSA22 proto-cluster region.

et al. 2004; Yang et al. 2009; Yang et al. 2010), suggestive of disappearing LABs at  $z \gtrsim 6$ . Similar to Shibuya et al. (2016), we fit the Madau-Lilly plot-type formula,

$$N_{\text{LAB}}(z) = a \times \frac{(1+z)^b}{1 + [(1+z)/c]^d}, \quad (5)$$

where  $a, b, c$ , and  $d$  are free parameters (Madau & Dickinson 2014) to our  $N_{\text{LAB}}$  evolution. For the fitting, we exclude Matsuda et al. (2009)'s data point which has been obtained in an overdense region, SSA22. The best-fit parameters are  $a = 9.1 \times 10^{-8}$ ,  $b = 2.9$ ,  $c = 5.0$ , and  $d = 11.7$ . In our large-area search for LABs at  $z \simeq 6-7$ , we identify, for the first time, the  $N_{\text{LAB}}$  evolutionary trend which is similar to the Madau-Lilly SFRD plot.

However, it should be noted that the LAB selection method is not homogeneous in our comparison of  $N_{\text{LAB}}$  at  $z \simeq 0-7$ . There is a possibility that the  $N_{\text{LAB}}$  evolution from  $z \simeq 7$  to  $z \simeq 3$  is caused by the cosmological surface brightness dimming effect at high- $z$ . The cosmological surface brightness dimming

would significantly affect the detection and selection completeness for LABs at high- $z$ . To confirm the  $N_{\text{LAB}}$  evolution, we need to homogenize the selection method for LABs at  $z \simeq 2-7$  in the future HSC NB data.

## 7 Summary and Conclusions

We develop an unprecedentedly large catalog consisting of LAEs at  $z = 5.7$  and  $6.6$  that are identified by the SILVERRUSH program with the first NB imaging data of the Subaru/HSC survey. The NB imaging data is about an order of magnitude larger than any other surveys for  $z \simeq 6-7$  LAEs conducted to date.

Our findings are as follows:

- We identify 2,354  $\gtrsim L^*$  LAEs at  $z = 5.7$  and  $6.6$  on the 13.8 and 21.2  $\text{deg}^2$  sky, respectively. We confirm that the LAE catalog is reliable on the basis of 97 LAEs whose spectroscopic redshifts are already determined by this program (Shibuya et al. 2017b) and the previous studies (e.g., Mallery et al. 2012). The LAE catalog is presented in this work, and published online.
- With the large LAE catalog, we derive the rest-frame Ly $\alpha$  EW distributions of LAEs at  $z \simeq 5.7$  and  $\simeq 6.6$  that are reasonably explained by the exponential profiles with the scale lengths of  $72 \pm 19$  and  $119 \pm 4 \text{ \AA}$ , respectively, showing the increase trend towards high- $z$ . We find  $\sim 700$  LAEs with a LEW of  $\gtrsim 240 \text{ \AA}$  that are candidates of young-metal poor galaxies and AGNs, and the fraction of the LEW LAEs to all LAEs is moderately large,  $\sim 30\%$ .
- Our LAE catalog includes 11 LABs that are LAEs with spatially extended Ly $\alpha$  emission whose profile is clearly distinguished from those of stellar objects at the  $\gtrsim 3\sigma$  level. The number density of the LABs at  $z \simeq 6-7$  is  $\sim 10^{-7} - 10^{-6} \text{ Mpc}^{-3}$  that is  $\sim 10-100$  times lower than those claimed for LABs at  $z \simeq 2-3$ , suggestive of disappearing LABs at  $z \gtrsim 6$ , albeit with the different selection methods and criteria for the low and high- $z$  LABs.

It should be noted that Ly $\alpha$  EW scale length derivation methods and the LAB selections are not homogeneous in a redshift range of  $z \simeq 0-7$ . Using the future  $z \simeq 2.2, 5.7, 6.6$ , and  $7.3$  HSC NB data, we will systematically investigate the redshift evolution of Ly $\alpha$  EW scale lengths and  $N_{\text{LAB}}$  at  $z \simeq 2-7$  in

homogeneous methods.

## Acknowledgments

We would like to thank James Bosch, Richard S. Ellis, Masao Hayashi, Robert H. Lupton, Michael A. Strauss for useful discussion and comments. This work is based on observations taken by the Subaru Telescope and the Keck telescope which are operated by the National Observatory of Japan. This work was supported by World Premier International Research Center Initiative (WPI Initiative), MEXT, Japan, KAKENHI (23244025) and (21244013) Grant-in-Aid for Scientific Research (A) through Japan Society for the Promotion of Science (JSPS), and an Advanced Leading Graduate Course for Photon Science grant. The NB816 filter was supported by Ehime University (PI: Y. Taniguchi). The NB921 filter was supported by KAKENHI (23244025) Grant-in-Aid for Scientific Research (A) through the Japan Society for the Promotion of Science (PI: M. Ouchi). NK is supported by the JSPS grant 15H03645.

The Hyper Suprime-Cam (HSC) collaboration includes the astronomical communities of Japan and Taiwan, and Princeton University. The HSC instrumentation and software were developed by the National Astronomical Observatory of Japan (NAOJ), the Kavli Institute for the Physics and Mathematics of the Universe (Kavli IPMU), the University of Tokyo, the High Energy Accelerator Research Organization (KEK), the Academia Sinica Institute for Astronomy and Astrophysics in Taiwan (ASIAA), and Princeton University. Funding was contributed by the FIRST program from Japanese Cabinet Office, the Ministry of Education, Culture, Sports, Science and Technology (MEXT), the Japan Society for the Promotion of Science (JSPS), Japan Science and Technology Agency (JST), the Toray Science Foundation, NAOJ, Kavli IPMU, KEK, ASIAA, and Princeton University.

This paper makes use of software developed for the Large Synoptic Survey Telescope. We thank the LSST Project for making their code available as free software at <http://dm.lsst.org>

The Pan-STARRS1 Surveys (PS1) have been made possible through contributions of the Institute for Astronomy, the University of Hawaii, the Pan-STARRS Project Office, the Max-Planck Society and its participating institutes, the Max Planck Institute for Astronomy, Heidelberg and the Max Planck Institute for Extraterrestrial Physics, Garching, The Johns Hopkins University, Durham University, the University of Edinburgh, Queen's University Belfast, the Harvard-Smithsonian Center for Astrophysics, the Las Cumbres Observatory Global Telescope Network Incorporated, the National Central University of Taiwan, the Space Telescope Science Institute, the National Aeronautics and Space Administration under Grant No. NNX08AR22G issued through the Planetary Science Division of the NASA Science Mission Directorate, the National Science Foundation under Grant No. AST-1238877, the University of Maryland, and Eotvos Lorand University (ELTE) and the Los Alamos National Laboratory.

Based on data collected at the Subaru Telescope and retrieved from the HSC data archive system, which is operated by Subaru Telescope and Astronomy Data Center at National Astronomical Observatory of Japan.

## References

- Aihara, H., et al. 2017a, ArXiv e-prints  
 —. 2017b, ArXiv e-prints  
 Ajiki, M., et al. 2002, ApJL, 576, L25  
 Arrigoni Battaia, F., Hennawi, J. F., Prochaska, J. X., & Cantalupo, S. 2015a, ApJ, 809, 163  
 Arrigoni Battaia, F., Yang, Y., Hennawi, J. F., Prochaska, J. X., Matsuda, Y., Yamada, T., & Hayashino, T. 2015b, ApJ, 804, 26  
 Axelrod, T., Kantor, J., Lupton, R. H., & Pierfederici, F. 2010, An open source application framework for astronomical imaging pipelines  
 Bertin, E., & Arnouts, S. 1996, A&AS, 117, 393  
 Blanc, G. A., et al. 2011, ApJ, 736, 31  
 Bond, N. A., Gawiser, E., Guaita, L., Padilla, N., Gronwall, C., Ciardullo, R., & Lai, K. 2012, ApJ, 753, 95  
 Bosch, J., et al. 2017, to be submitted to PASJ  
 Cai, Z., et al. 2017, ApJ, 837, 71  
 Cantalupo, S., Arrigoni-Battaia, F., Prochaska, J. X., Hennawi, J. F., & Madau, P. 2014, Nature, 506, 63  
 Cantalupo, S., Porciani, C., Lilly, S. J., & Miniati, F. 2005, ApJ, 628, 61  
 Ciardullo, R., et al. 2012, ApJ, 744, 110  
 Cowie, L. L., Barger, A. J., & Hu, E. M. 2010, ApJ, 711, 928  
 Cowie, L. L., Hu, E. M., & Songaila, A. 2011, ApJL, 735, L38  
 Dressler, A., Martin, C. L., Henry, A., Sawicki, M., & McCarthy, P. 2011, ApJ, 740, 71  
 Duval, F., Schaerer, D., Östlin, G., & Laursen, P. 2013, ArXiv e-prints  
 Erb, D. K., Bogosavljević, M., & Steidel, C. C. 2011, ApJL, 740, L31  
 Finkelstein, S. L., Rhoads, J. E., Malhotra, S., Grogan, N., & Wang, J. 2008, ApJ, 678, 655  
 Finkelstein, S. L., Rhoads, J. E., Malhotra, S., Pirzkal, N., & Wang, J. 2007, ApJ, 660, 1023  
 Gawiser, E., et al. 2007, ApJ, 671, 278  
 Gronwall, C., et al. 2007, ApJ, 667, 79  
 Guaita, L., et al. 2011, ApJ, 733, 114  
 Haiman, Z., Abel, T., & Rees, M. J. 2000, ApJ, 534, 11  
 Hansen, M., & Oh, S. P. 2006, mnras, 367, 979  
 Harikane, Y., et al. 2017, ArXiv e-prints  
 Hashimoto, T., et al. 2017, MNRAS, 465, 1543  
 Hayes, M., Scarlata, C., & Siana, B. 2011, Nature, 476, 304  
 Hennawi, J. F., Prochaska, J. X., Cantalupo, S., & Arrigoni-Battaia, F. 2015, Science, 348, 779  
 Hu, E. M., Cowie, L. L., Barger, A. J., Capak, P., Kakazu, Y., & Trouille, L. 2010, ApJ, 725, 394  
 Ivezić, Z., et al. 2008, ArXiv e-prints  
 Jurić, M., et al. 2015, ArXiv e-prints  
 Kashikawa, N., et al. 2006, ApJ, 648, 7  
 —. 2011, ApJ, 734, 119  
 —. 2012, ApJ, 761, 85  
 Kawanomoto, S. 2017, to be submitted to PASJ  
 Keel, W. C., White, III, R. E., Chapman, S., & Windhorst, R. A. 2009, AJ, 138, 986  
 Kodaira, K., et al. 2003, PASJ, 55, L17  
 Kojima, T., Ouchi, M., Nakajima, K., Shibuya, T., Harikane, Y., & Ono, Y. 2016, ArXiv e-prints  
 Konno, A., et al. 2014, apj, 797, 16  
 —. 2017, to be submitted to PASJ  
 Kusakabe, H., Shimasaku, K., Nakajima, K., & Ouchi, M. 2015, ApJL, 800, L29  
 Laursen, P., Duval, F., & Östlin, G. 2013, ApJ, 766, 124  
 Laursen, P., & Sommer-Larsen, J. 2007, ApJL, 657, L69  
 Laursen, P., Sommer-Larsen, J., & Andersen, A. C. 2009, ApJ, 704, 1640  
 Lilly, S. J., Le Fevre, O., Hammer, F., & Crampton, D. 1996, ApJL, 460, L1  
 Madau, P., & Dickinson, M. 2014, ARA&A, 52, 415  
 Madau, P., Ferguson, H. C., Dickinson, M. E., Giavalisco, M., Steidel,

- C. C., & Fruchter, A. 1996, *MNRAS*, 283, 1388
- Magnier, E. A., et al. 2013, *ApJS*, 205, 20
- Malhotra, S., & Rhoads, J. E. 2002, *ApJL*, 565, L71
- . 2004, *ApJl*, 617, L5
- Mallery, R. P., et al. 2012, *ApJ*, 760, 128
- Matsuda, Y., et al. 2004, *AJ*, 128, 569
- . 2009, *MNRAS*, 400, L66
- . 2011, *MNRAS*, 410, L13
- Matthee, J., Sobral, D., Santos, S., Röttgering, H., Darvish, B., & Mobasher, B. 2015, *mras*, 451, 400
- Murayama, T., et al. 2007, *ApJS*, 172, 523
- Nagao, T., et al. 2008, *ApJ*, 680, 100
- Nakajima, K., & Ouchi, M. 2014, *MNRAS*, 442, 900
- Nakajima, K., Ouchi, M., Shimasaku, K., Hashimoto, T., Ono, Y., & Lee, J. C. 2013, *ApJ*, 769, 3
- Nakajima, K., et al. 2012, *ApJ*, 745, 12
- Neufeld, D. A. 1991, *ApJl*, 370, L85
- Nilsson, K. K., Tapken, C., Møller, P., Freudling, W., Fynbo, J. P. U., Meisenheimer, K., Laursen, P., & Östlin, G. 2009, *A&A*, 498, 13
- Oke, J. B., & Gunn, J. E. 1983, *ApJ*, 266, 713
- Ono, Y., et al. 2010, *MNRAS*, 402, 1580
- . 2017, ArXiv e-prints
- Ota, K., et al. 2017, ArXiv e-prints
- Ouchi, M., et al. 2008, *ApJs*, 176, 301
- . 2009, *ApJ*, 696, 1164
- . 2010, *ApJ*, 723, 869
- . 2017, ArXiv e-prints
- Oyarzún, G. A., et al. 2016, *ApJL*, 821, L14
- Planck Collaboration et al. 2016, *A&A*, 594, A13
- Saito, T., Shimasaku, K., Okamura, S., Ouchi, M., Akiyama, M., & Yoshida, M. 2006, *ApJ*, 648, 54
- Salpeter, E. E. 1955, *ApJ*, 121, 161
- Schlafly, E. F., et al. 2012, *ApJ*, 756, 158
- Shibuya, T., Kashikawa, N., Ota, K., Iye, M., Ouchi, M., Furusawa, H., Shimasaku, K., & Hattori, T. 2012, *ApJ*, 752, 114
- Shibuya, T., Ouchi, M., Kubo, M., & Harikane, Y. 2016, *ApJ*, 821, 72
- Shibuya, T., Ouchi, M., Nakajima, K., Yuma, S., Hashimoto, T., Shimasaku, K., Mori, M., & Umemura, M. 2014, ArXiv e-prints
- Shibuya, T., et al. 2017b, to be submitted to PASJ
- Shimasaku, K., et al. 2006, *PASJ*, 58, 313
- Sobral, D., Matthee, J., Darvish, B., Schaerer, D., Mobasher, B., Röttgering, H. J. A., Santos, S., & Hemmati, S. 2015, *apj*, 808, 139
- Steidel, C. C., Adelberger, K. L., Shapley, A. E., Pettini, M., Dickinson, M., & Giavalisco, M. 2000, *ApJ*, 532, 170
- Takada, M., et al. 2017, to be submitted to PASJ
- Taniguchi, Y., & Shioya, Y. 2000, *ApJL*, 532, L13
- Taniguchi, Y., et al. 2005, *PASJ*, 57, 165
- . 2009, *ApJ*, 701, 915
- Tonry, J. L., et al. 2012, *ApJ*, 750, 99
- Yajima, H., Li, Y., & Zhu, Q. 2013, *ApJ*, 773, 151
- Yajima, H., Li, Y., Zhu, Q., Abel, T., Gronwall, C., & Ciardullo, R. 2012, ArXiv e-prints
- Yang, Y., Zabludoff, A., Eisenstein, D., & Davé, R. 2010, *ApJ*, 719, 1654
- Yang, Y., Zabludoff, A., Tremonti, C., Eisenstein, D., & Davé, R. 2009, *ApJ*, 693, 1579
- Zheng, Z., Cen, R., Trac, H., & Miralda-Escudé, J. 2010, *ApJ*, 716, 574
- Zheng, Z., & Wallace, J. 2013, ArXiv e-prints
- Zheng, Z.-Y., Wang, J.-X., Malhotra, S., Rhoads, J. E., Finkelstein, S. L., & Finkelstein, K. 2014, *MNRAS*, 439, 1101
- Zheng, Z.-Y., et al. 2017, ArXiv e-prints